

Probing *In Vivo* Trafficking of Polymer/DNA Micellar Nanoparticles Using SPECT/CT Imaging

Rajesh R Patil¹, Jianhua Yu², Sangeeta R Banerjee², Yong Ren¹, Derek Leong¹, Xuan Jiang¹, Martin Pomper², Benjamin Tsui², Dara L Kraitchman^{2,3} and Hai-Quan Mao^{1,4}

¹Department of Materials Science and Engineering, Whiting School of Engineering, Johns Hopkins University, Baltimore, Maryland, USA;

²Russell H. Morgan Department of Radiology and Radiological Science, Johns Hopkins University School of Medicine, Baltimore, Maryland, USA;

³Department of Molecular and Comparative Pathobiology, Johns Hopkins University School of Medicine, Baltimore, Maryland, USA;

⁴Translational Tissue Engineering Center, Whitaker Biomedical Engineering Institute, Johns Hopkins School of Medicine, Baltimore, Maryland, USA

Successful translation of nonviral gene delivery to therapeutic applications requires detailed understanding of *in vivo* trafficking of the vehicles. This report compares the pharmacokinetic and biodistribution profiles of polyethylene glycol-*b*-polyphosphoramidate (PEG-*b*-PPA)/DNA micellar nanoparticles after administration through intravenous infusion, intrabiliary infusion, and hydrodynamic injection using single photon emission computed tomography/computed tomography (SPECT/CT) imaging. Nanoparticles were labeled with ¹¹¹In using an optimized protocol to retain their favorable physicochemical properties. Quantitative imaging analysis revealed different *in vivo* trafficking kinetics for PEG-*b*-PPA/DNA nanoparticles after different routes of administration. The intrabiliary infusion resulted in the highest liver uptake of micelles compared with the other two routes. Analysis of intrabiliary infusion by the two-compartment pharmacokinetic modeling revealed efficient retention of micelles in the liver and minimal micelle leakage from the liver to the blood stream. This study demonstrates the utility of SPECT/CT as an effective noninvasive imaging modality for the characterization of nanoparticle trafficking *in vivo* and confirms that intrabiliary infusion is an effective route for liver-targeted delivery of DNA-containing nanoparticles.

Received 9 December 2010; accepted 31 May 2011; published online 12 July 2011. doi:10.1038/mt.2011.128

INTRODUCTION

The physicochemical properties of DNA-containing nanoparticles in physiological media are important determinants for their *in vivo* trafficking and gene delivery efficiency.^{1,2} Poor control over nanoparticle stability in serum-containing media remains a significant challenge to successful delivery to target tissue. We have recently developed a series of polyethylene glycol-*b*-polyphosphoramidate (PEG-*b*-PPA)/DNA micellar nanoparticles that exhibit favorable serum and bile stabilities for liver-targeted gene delivery.^{3–6} On the other hand, the route of administration for nanoparticle gene carriers also significantly influences its pharmacodynamic profile,

as the trafficking patterns (pharmacokinetics and biodistribution profile) of nanoparticles following various routes of administration are distinctly different depending on the tissue structures and physiological milieu to which the particles are delivered.⁷ In order to reach the target site/cells, nanoparticles have to bypass a number of anatomical and biological barriers.^{7–9} Identifying these rate-limiting steps through analysis of pharmacokinetic profile can offer important guidance to engineer safe and effective nanoparticle gene carriers. The pharmacokinetic and biodistribution profiles of drug and gene delivery carriers are traditionally determined using radiolabeling techniques, such as radiolabeling DNA^{8,9} or polymer¹⁰ followed by quantification of radioactivity in each organ, or by quantification of DNA using real-time PCR.¹¹ These methods are highly labor intensive and require sacrificing a large number of animals to obtain data at various time points.

Noninvasive *in vivo* imaging has emerged as a valuable tool for identifying the fate of drug/gene delivery systems in tissues, quantifying injected dose in various organs, and probing toxicity.^{12–14} Fluorescence imaging,¹⁵ near-infrared imaging,¹⁶ magnetic resonance imaging,¹¹ and nuclear imaging^{16–18} are frequently used imaging modalities for this purpose. The nuclear imaging approaches, such as single photon emission computed tomography (SPECT) and positron emission tomography (PET)^{13,17} have the advantages of high-intrinsic sensitivity, large depth of tissue penetration, and the availability of a broad range of clinically tested imaging agents. The chemistry of radionuclides used in nuclear imaging has been well studied. Using these radiochemistry techniques, it is feasible to radiolabel a component of the delivery system and generate the pharmacokinetic and biodistribution profiles. Furthermore, integration of computed tomography (CT) with SPECT or PET allows for direct fusion of X-ray anatomical information and radionuclide functional imaging information, and offers a high temporal and spatial resolution critical to determining pharmacokinetics in different organs and to generating an organ distribution profile of a given delivery system.^{18,19}

Gene delivery to the liver remains a formidable challenge. For nearly all reported gene carriers given by intravenous injection or intraportal infusion, only a small fraction of the administered dose can reach the targeted liver tissue and hepatocytes.²⁰ We have shown that the liver-targeted delivery efficiency of polymer/DNA

Correspondence: Hai-Quan Mao, Department of Materials Science and Engineering, Whiting School of Engineering, Johns Hopkins University, 102 Maryland Hall, 3400 N. Charles Street, Baltimore, Maryland 21218, USA. E-mail: hmao@jhu.edu

nanoparticles was dependent on the route of administration. PEG-*b*-PPA/DNA micelles administered by intrabiliary infusion were much more efficient in eliciting transgene expression in liver than intraportal or intravenous infusion.²¹ On the other hand, hydrodynamic injection of plasmid DNA has been regarded as the experimental bench mark for liver-targeted gene delivery.²² In this study, we aim to quantitatively compare the *in vivo* pharmacokinetic profiles of PEG-*b*-PPA/DNA micelles after three different routes of administration (intravenous infusion, intrabiliary infusion, and hydrodynamic injection) using the SPECT/CT imaging method, and provide insights into anatomical and biological barriers for effective delivery of DNA micelles to the liver. The trafficking of micelles after intrabiliary infusion was further investigated by two-compartmental modeling.

RESULTS

Radiolabeling of PEG-*b*-PPA polymer

To label PEG_{12k}-*b*-PPA_{68k} (hereafter referred to as PEG-*b*-PPA) with In-111, DTPA as a chelator for ¹¹¹In³⁺ was first conjugated to the polymer (Supplementary Figure S1). To optimize the grafting degree of DTPA, we varied the feeding ratio of *p*-SCN-Bn-DTPA to total amino groups in polymer from 1 to 20% (1, 2, 6, 10, and 20%), and characterized the DTPA-grafting degrees from ¹H-NMR spectra using the characteristic resonance peaks of defining structural attributes of Bn-DTPA moieties (δ7.25–7.16, 3.38, 2.94, and 2.61 p.p.m., Supplementary Figure S2). The obtained DTPA-grafting degrees were 0.11, 0.89, 2.93, 5.24, and 8.82%, corresponding to the *p*-SCN-Bn-DTPA feeding ratio of 1, 2, 6, 10, and 20%, respectively.

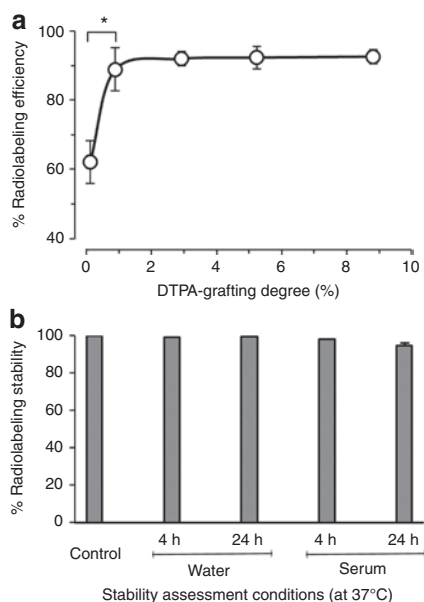


Figure 1 Optimization of radiolabeling of polyethylene glycol-*b*-polyphosphoramidate (PEG-*b*-PPA). **(a)** Effect of DTPA-grafting degree on radiolabeling efficiency of the polymer (mean \pm SD of mean, $n = 3$, $*P < 0.01$). The DTPA-grafting degree was analyzed by ¹H-NMR. **(b)** The stability of radiolabeled PEG-*b*-PPA in water and 10% fetal serum albumin-containing medium at 37°C for 4 and 24 hours, respectively. The radiolabeling stability was estimated using thin-layer chromatography. The freshly prepared radiolabeled polymer was used as the control.

Radiolabeling of PEG-*b*-PPA was achieved by incubating ¹¹¹In³⁺ with DTPA-conjugated PEG-*b*-PPA with different grafting degrees. Thin-layer chromatography revealed similar radiolabeling efficiency (85–90%) for DTPA-conjugated polymers with grafting degrees between 0.89 and 8.82% (unpaired Student's *t*-test, $P > 0.05$) (Figure 1a). However, DTPA-grafting degree of <0.89% showed significantly reduced radiolabeling efficiency (unpaired *t*-test, $P < 0.01$). The radiochemical purity of ¹¹¹In-labeled DTPA-PEG-*b*-PPA was determined using size exclusion chromatography using dual UV and radioactivity detectors. The overlapped UV-radioactivity chromatograms indicated that all polymer fractions are labeled with ¹¹¹In with no additional radioactive fractions or unconjugated *p*-SCN-Bn-DTPA (Supplementary Figure S3). This result validated the effective labeling protocol and purification method by ultracentrifugation.

The stability of radiolabeled polymer was evaluated in 10% fetal bovine serum at 37°C before preparing micelles with plasmid DNA. No significant loss of radiolabel from the polymer conjugate was observed after being incubated in water for 24 hours at 37°C or in 10% serum for 4 hours. However, minor loss (5.2%) was detected after incubating in 10% serum at 37°C for 24 hours (Figure 1b).

Physicochemical characterization of radiolabeled DNA micelles

To assess the effect of ¹¹¹In labeling on DNA condensation and on physicochemical properties of the micelles, the nonradioactive indium-labeled PEG-*b*-PPA/DNA micelles were prepared using

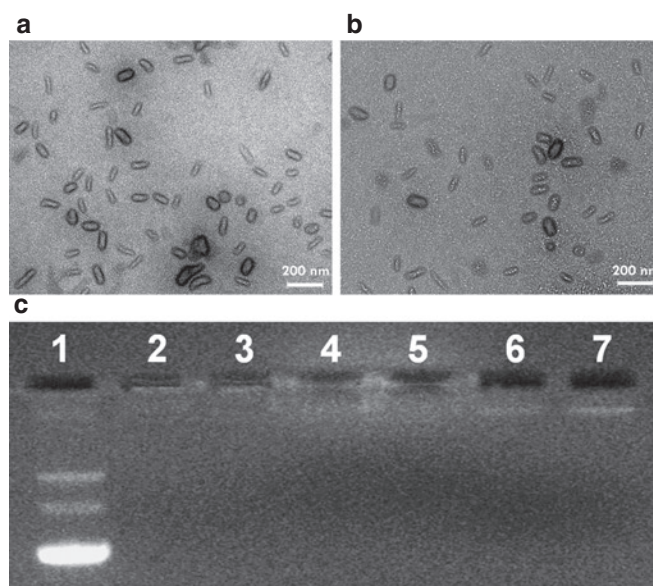


Figure 2 Effect of radiolabeling on size, morphology, and stability of PEG-*b*-PPA/DNA micellar nanoparticles. TEM images of **(a)** unlabeled micelles and **(b)** ¹¹¹In-labeled micelles (Bars = 200 nm). **(c)** Stabilities of unlabeled and labeled micelles in 0.15 mol/l NaCl or 10% fetal bovine serum (FBS) by gel retardation assay. Lane 1: plasmid DNA; lane 2: unlabeled micelles; lane 3: radiolabeled micelles; lanes 4 and 5: unlabeled and labeled micelles, respectively, after incubation in 0.15 mol/l NaCl solution for 1 hour at 37°C; lanes 6 and 7: unlabeled and labeled micelles, respectively, after incubation in 10% FBS-containing medium for 1 hour at 37°C.

the same protocol except replacing the $^{111}\text{In}^{3+}$ with nonradioactive In^{3+} . The physiochemical properties of these micelles were compared against unlabeled PEG-*b*-PPA micelles. The micelles formed at the same N/P ratio with unlabeled or labeled polymer showed similar morphology (Figure 2a,b), size (67.2 ± 14.9 nm and 72.4 ± 5.5 nm for unlabeled and labeled micelles, respectively) and surface charge (38.6 ± 0.98 mV and 35.2 ± 3.55 mV for unlabeled and labeled micelles, respectively) (unpaired *t*-test, $P > 0.05$). The gel retardation assay to evaluate the stability of micelles revealed no release of DNA from labeled micelles or unlabeled micelles after being challenged with 0.15 mol/l NaCl or 10% serum for 1 hour (Figure 2c).

Validation of SPECT/CT imaging data

In this study, the calibration factor that converts SPECT image pixel intensity to *in vivo* radioactivity was generated from a phantom test and applied to the imaging analysis for radioactivity determination in the animal study. The results of the phantom test are described in the **Supplementary Figure S4**. We analyzed the data obtained from SPECT imaging experiments using the calibration equation generated from the phantom test. This data processing and analysis method were validated by comparing the SPECT/CT imaging data with a parallel experiment to generate the pharmacokinetic and biodistribution profiles using gamma-counting of blood samples at different time intervals and tissue samples collected after the animals were sacrificed. In this experiment, micelles were infused through intravenous administration. As shown in Figure 3, the pharmacokinetic and biodistribution profiles obtained with the gamma-counting and

SPECT/CT imaging analysis were comparable (paired *t*-test, $P > 0.05$).

In vivo trafficking of DNA micelles after three different routes of administration

The effect of different routes of administration on the *in vivo* trafficking of DNA micelles are depicted in Figures 3 and 4. The 3-D nanoparticle distribution images rendered from whole-body scans can be accessed at the journal website (**Supplementary Materials and Methods** and **Supplementary Videos S1–S3**). For the intravenous infusion of nanoparticles, because the infusion lasted for 20 minutes, the maximum tissue deposition concentrations of the infused PEG-*b*-PPA/DNA micelles were observed at the completion of the infusion (Figure 3a,c), reaching a maximum blood concentration (C_{max}) of $1.09 \pm 0.1\%$ of injected dose/ml. These intravenously infused nanoparticles were cleared quickly from the blood over the next 80 minutes or so. Surprisingly, the majority of the infused micelles were taken up avidly by the liver (Figure 3b). No significant accumulation of nanoparticles was observed in the lung whereas minor uptake of DNA micelles was observed in the spleen and kidney. The whole-body SPECT/CT images corroborated well with the biodistribution data (Figure 3b,c). These results implied that these micellar nanoparticles showed minimal aggregation and good serum stability.

Following hydrodynamic injection, $90.23 \pm 4.08\%$ of the total injected micelles were found to be taken up by the liver and minor fractions were taken up by the spleen and kidney ($1.19 \pm 0.11\%$ and $3.14 \pm 0.48\%$ of total dose, respectively, Figure 4a,c). The kinetics of radiolabeled micelles in the blood was fitted using a

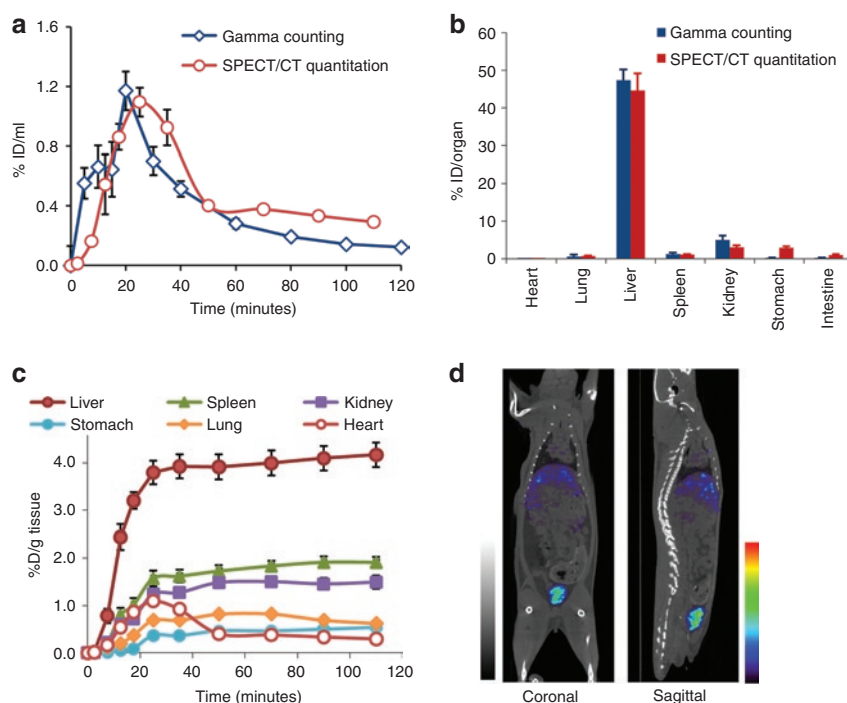


Figure 3 *In vivo* trafficking of radiolabeled micelles following intravenous infusion. (a) Pharmacokinetic profiles and (b) biodistribution profiles of radiolabeled micelles administered through intravenous infusion obtained by single photon emission computed tomography/computed tomography (SPECT/CT) and gamma-counting (mean \pm SD of mean, $n = 4$). (c) Time intensity curves in different organs by SPECT/CT quantification of micelles infused by intravenous infusion in rats (mean \pm SD of mean, $n = 4$). (d) Whole-body images (gray scale: CT, pseudo-color map: SPECT) of a rat at 2 hours postinfusion. The rendered 3-D images can be accessed in **Supplementary Video S1**.

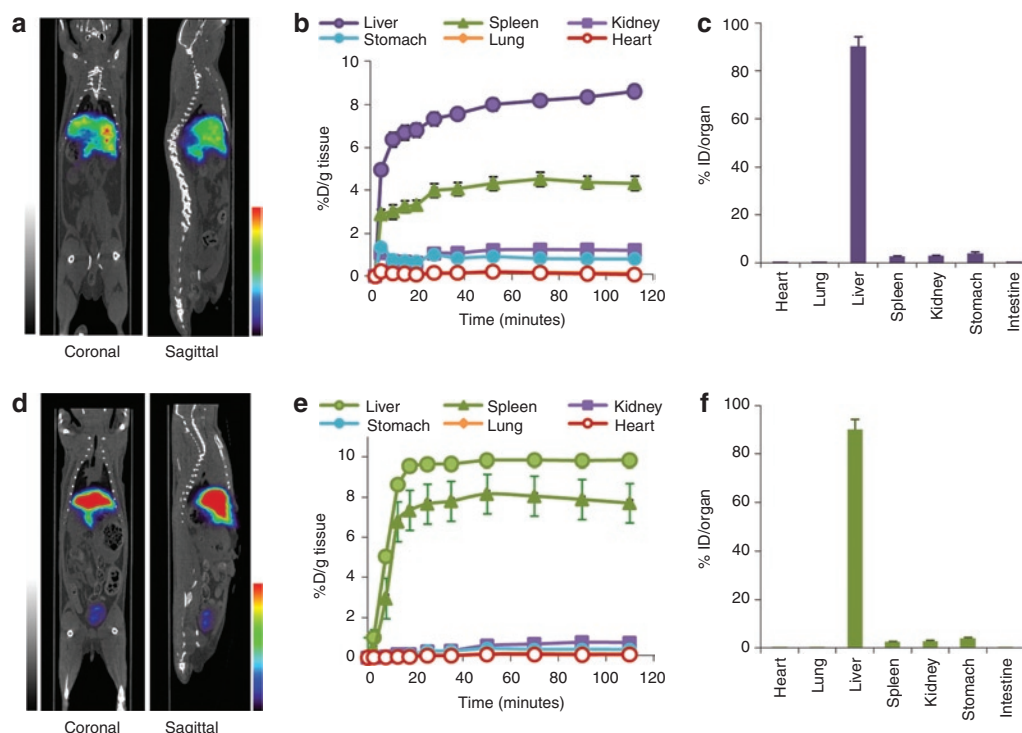


Figure 4 *In vivo* trafficking of radiolabeled micelles following hydrodynamic injection and intrabiliary infusion. Whole-body images [a and d, gray scale, CT images; pseudo-color, single photon emission computed tomography (SPECT) images], (b, e) time intensity curves and (c, f) biodistribution profiles of labeled micelles in different organs (mean \pm s.e. of mean, $n = 3$) of a rat at 2.02 hours and 2 hours after administration through (a–c) hydrodynamic injection and (d–f) intrabiliary infusion, respectively. Same color schemes were used for all SPECT imaging analysis. The compassed appearance of the liver in (d) was due to the use of cotton balls to push the liver backwards for the ease of visualization and infusion into the common bile duct. The rendered 3-D images can be accessed in **Supplementary Videos S2** and **S3**.

Table 1 Pharmacokinetic data generated by noncompartmental fitting of blood–time activity profiles after different routes of administration

Parameter	Hydrodynamic injection	Intravenous infusion	Intrabiliary infusion
Terminal elimination rate constant in blood compartment (λ_z , min^{-1})	$(17.2 \pm 6.5) \times 10^{-3}$	$(7.0 \pm 3.0) \times 10^{-3}$	$(2.8 \pm 1.0) \times 10^{-3}$
Half-life of the elimination phase ($t_{1/2}$, minutes)	46.7 ± 16.0	108.1 ± 65.6	325.9 ± 83.2
Time of peak (t_{max} , minutes)	N.D.	25.0 ± 0	63.3 ± 5.8
Peak plasma concentration (C_{max} , %ID·ml $^{-1}$)	N.D.	1.10 ± 0.97	0.17 ± 0.02
C_t/C_{max} at 2 hours	N.D.	0.27 ± 0.01	0.96 ± 0.03
Area under the plasma concentration–time curve at 2 hours (AUC_{0-2} , %ID·minute/ml)	17.1 ± 4.3	54.3 ± 2.9	13.5 ± 2.1
Area under the plasma concentration–time curve extrapolated to infinity ($\text{AUC}_{0-\infty}$, %ID·minute/ml)	24.1 ± 6.2	138.5 ± 34.7	91.7 ± 30.3
$\text{AUC}_{0-2}/\text{AUC}_{0-\infty}$	0.85 ± 0.10	0.47 ± 0.12	0.19 ± 0.05
Mean resident time in blood compartment ($\text{MRT}_{0-\infty}$, minutes)	47.2 ± 22.0	242.0 ± 80.2	489.9 ± 119.3
Volume of distribution (V_d , TD/%ID/ml)	391.1 ± 153.4	172.7 ± 30.7	554.5 ± 73.8
Total body clearance rate (Cl_{obs} , TD·ml/%ID/minute)	4.94 ± 1.93	0.90 ± 0.28	1.58 ± 0.60
Volume of distribution at steady state (V_{ss} , TD·%ID $^{-1}$ ·ml)	501.1 ± 186.4	160.3 ± 22.0	585.9 ± 77.8

Abbreviations: C_t , observed concentration at time t ; ID, injected dose; N.D., not determined; TD, total dose measured.

ND in case of hydrodynamic injection, due to the 2-minute interval between injection and initiation of scan, the values for C_{max} , t_{max} could not be determined.

noncompartmental pharmacokinetic model and the values are depicted in **Table 1**. For hydrodynamic infusion, due to rapid deposition to the liver, low blood concentration was detected. This resulted in the highest terminal elimination rate constant ($\lambda_z = (17.2 \pm 6.5) \times 10^{-3}/\text{minute}$) and total body clearance ($Cl_{\text{obs}} = 4.94 \pm 1.93$ TD ml/%ID/minute) values.^{11,23} The rapid clearance from the blood and hence the lowest blood retention

was reflected by the lowest area under the plasma concentration–time curve value when extrapolated to infinity ($\text{AUC}_{0-\infty}$, 24.1 %ID·minute/ml), the lowest mean resident time ($\text{MRT}_{0-\infty} = 47.2 \pm 22.0$ minute), and the highest $\text{AUC}_{0-2}/\text{AUC}_{0-\infty}$ ratio amongst the three administration routes evaluated (**Table 1**).

Similar to the hydrodynamic infusion, intrabiliary infusion of the radiolabeled micelles also resulted in dominant total liver

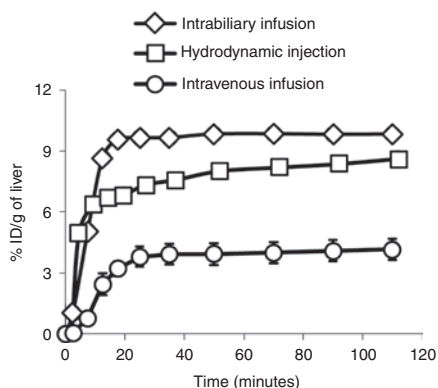


Figure 5 Comparison of time courses of DNA micelle deposition in the liver after three different routes of administration determined by single photon emission computed tomography/computed tomography (SPECT/CT) quantification (mean \pm s.e. of mean, $n = 3$).

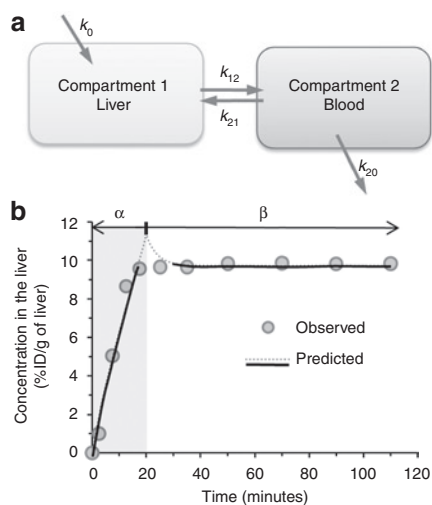


Figure 6 Analysis of micelle concentration in the liver by the two-compartment pharmacokinetics model constructed for intrabiliary infusion of DNA micelles. **(a)** Description of the compartments. **(b)** Model fit of liver concentration profile from **Figure 5** and data generated by the two-compartment model analysis.

deposition, while the distribution to other organs was negligible (**Figure 4d–f**). Pharmacokinetics analysis of the SPECT/CT data (**Table 1**) implied that micelles maintained very low but steady levels in the blood as indicated by lower peak plasma concentration ($C_{\max} = 0.17 \pm 0.02\%$ ID/ml) and higher C_{2h}/C_{\max} ratio (0.96 ± 0.03), but also the lowest terminal elimination rate constant ($\lambda_z = (2.8 \pm 1.0) \times 10^{-3}/\text{minute}$), the highest $AUC_{0-\infty}$, and longest mean resident time ($MRT_{0-\infty} = 489.9 \pm 119.3$ minutes). The highest uptake of micelles in the liver after intrabiliary infusion is also reflected by the highest V_d and V_{ss} .

Liver uptake of micelles after intrabiliary infusion

Considering the liver as a target site, we also compared the kinetics of radiolabeled micelles in the liver delivered by three different routes based on the collected SPECT/CT imaging data (**Figure 5**). The maximum liver concentration obtained after intrabiliary infusion ($C_{\max\text{-liver}} = 9.85 \pm 0.25\%$ ID/g tissue) was slightly higher than that obtained with hydrodynamic infusion

($8.62 \pm 0.19\%$ ID/g tissue), which was also reflected in the AUC_{0-2h} in the liver ($1,040.6 \pm 39.1\%$ ID·minute/g tissue and $859.4 \pm 41.7\%$ ID·minute/g tissue, respectively). Both values were more than twofold higher than those obtained for intravenous infusion ($C_{\max} = 4.16 \pm 0.26\%$ ID/g tissue, and $AUC_{0-2h} = 342.9 \pm 21.5\%$ ID·minute/g tissue in the liver). No statistically significant difference was observed between liver concentrations at 17.5 minutes and further time points after intrabiliary infusion.

Two-compartment modeling of pharmacokinetics of micelles after intrabiliary infusion

To further understand the trafficking of DNA micelles after intrabiliary infusion, the kinetics of micelles distribution in the liver was modeled using the standard two-compartmental analysis.^{23,24}

Figure 6a describes proposed two-compartment model where liver is considered as central compartment (compartment 1) as intrabiliary infusion results in direct administration of micelles to liver from which they are distributed to blood or other organs (compartment 2). We assumed that there is no lag time for the micelles to appear in liver following intrabiliary infusion, so k_0 is the infusion rate. The rate constants for distribution of from compartment 1 to 2 (K_{12}), redistribution from the blood compartment to the liver (K_{21}) and elimination from the blood compartment (K_{20}) are assumed first order.²⁴ The data was fitted in the two-compartment model using the PKsolver Program developed by Zhang *et al.*²⁵ The model was described by the mathematical equation:

when $t \leq t_{\text{inf}}$,

$$C(t) = A(1 - e^{-\alpha t}) + B(1 - e^{-\beta t})$$

when $t \geq t_{\text{inf}}$,

$$C(t) = A(e^{-\alpha(t-t_{\text{inf}})} - e^{-\alpha t}) + B(e^{-\beta(t-t_{\text{inf}})} - e^{-\beta t})$$

where $C(t)$ is the micelle concentration in the liver [percent of injected dose per gram tissue (%ID/g tissue)] at any given time t , t_{inf} (minute) is the infusion time, which is 20 minutes for this experiment, A (%ID/g) is the average micelle concentration in the liver during infusion phase (α phase, **Figure 6b**), α (min^{-1}) is the elimination constant of infusion phase, and is a function of K_{12} , K_{21} , and K_{20} .²⁴ B (%ID/g) is the average micelle concentration in the liver during the postinfusion phase (β phase), β (min^{-1}) is the elimination constant of the postinfusion phase, and is also a function of K_{12} , K_{21} , and K_{20} .

The fitted curves using this model and original data were plotted in **Figure 6b**. Various parameters calculated based on the model are listed in **Table 2**. The major fraction of dose was retained in the liver as indicated by the high average micelle concentrations in the liver during the infusion phase ($A = 8.79 \pm 0.58\%$ ID/g tissue) and postinfusion ($B = 9.68 \pm 0.60\%$ ID/g tissue) and the extremely low elimination rate constant ($\beta = 1 \times 10^{-6} \pm 6.57 \times 10^{-21}/\text{minute}$) and the high half-life ($t_{1/2, \beta} = 6.93 \times 10^6 \pm 4.55 \times 10^{-9}$ minutes) during the postinfusion phase as compared to those of the infusion phase ($\alpha = 0.30 \pm 0.05/\text{minute}$ and $t_{1/2, \alpha} = 2.40 \pm 0.34/\text{minutes}$). The overall rate of micelle leakage to the blood stream ($k_{12} = 0.11 \pm 0.04/\text{minutes}$) was similar to the rate of redistribution of micelles to the liver from the blood ($k_{21} = 0.14 \pm 0.01/\text{minute}$).

Table 2 Different parameters obtained after fitting the intrabiliary infusion data of radiolabeled micelles to a two-compartmental pharmacokinetics model

Fitted parameter	
Average concentration during infusion phase (A):	$8.79 \pm 0.58\%$ injected dose/g of tissue
Elimination constant of infusion phase (α)	$0.30 \pm 0.05/\text{minute}$
Half-life of infusion phase ($t_{1/2, \alpha}$)	2.40 ± 0.34 minutes
Average concentration postinfusion phase (B)	$9.68 \pm 0.60\%$ injected dose/g of tissue
Elimination constant postinfusion phase (β)	$1 \times 10^{-6} \pm 6.57 \times 10^{-21}/\text{minute}$
Half-life of postinfusion phase ($t_{1/2, \beta}$)	$6.93 \times 10^6 \pm 4.55 \times 10^{-9}/\text{minutes}$
Rate of infusion (k_0)	$5/\text{minute}$
Rate of distribution of micelles from the liver to the blood (K_{12})	$0.11 \pm 0.04/\text{minute}$
Rate of uptake of micelles from the blood to the liver (K_{21})	$0.14 \pm 0.01/\text{minute}$
Rate of elimination from the blood compartment (K_{20})	$(2.18 \pm 0.29) \times 10^{-6}/\text{min}$

DISCUSSION

The choice of micelle labeling method

Most studies evaluating the biodistribution of DNA nanoparticles using nuclear imaging modality label the polymer/lipid and not the DNA.¹⁰ DNA nanoparticles are formed by electrostatic interaction between cationic polymer/lipid and plasmid DNA, and might be prone to dissociation *in vivo* upon contact with high ionic strength buffers and charged macromolecules, hence resulting in misinterpretation of the biodistribution of DNA. Therefore we had preferred radiolabeling of the DNA over radiolabeling of the polymer. The DNA radiolabeling for SPECT imaging would require high specific radioactivity ($\sim 50 \mu\text{Ci}/\mu\text{g}$ DNA) in order to achieve a sufficient signal to noise ratio. We attempted radiolabeling of plasmid DNA by Mirus Bio Label IT reagent to introduce amino functional groups and further conjugating this amino group with *p*-SCN-Bn-DTPA. The DTPA moiety can be chelated with $^{111}\text{In}(\text{III})$ to produce radiolabeled DNA. However, the maximum specific radioactivity of labeled DNA we had obtained was $\sim 0.5 \mu\text{Ci}/\mu\text{g}$ DNA. Furthermore, the radiolabeled DNA was found to be highly unstable in presence of serum resulting in rapid loss of radiolabel. Therefore, we pursued radiolabeling of the polymer and ensured that radiolabeled polymer and micelles were sufficiently stable in serum-containing medium so that they could be used to reliably follow the pharmacokinetics of DNA micelles.

The radiolabeling protocol did not influence DNA micelle properties

In order to radiolabel PEG-*b*-PPA, DTPA was first conjugated to PEG-*b*-PPA as a chelator for $^{111}\text{In}^{3+}$. DTPA was conjugated using *p*-SCN-Bn-DTPA with a thiourea group that can react with side-chain amino groups in the PPA segment. Since the amino groups of the polymer are responsible for DNA condensation, it was important to minimize the impact of DTPA-conjugation on DNA-compaction ability of the polymer, whereas optimizing the

grafting degree of DTPA to achieve desired specific radioactivity of the labeled polymer and micelles. Radiolabeling study of DTPA-conjugated PEG-*b*-PPA revealed good radiolabeling efficiency ($>85\%$) for polymers conjugated with 0.89% DTPA or more, as compared with polymer with lower DTPA-conjugation degree (0.11%). Hence, 0.89% DTPA-conjugated PEG-*b*-PPA polymer was used for further study.

Sufficient stability of radiolabeled conjugate in serum is crucial for reliably characterizing the *in vivo* trafficking of nanoparticles. Incubating radiolabeled micelles with serum-containing media and water at 37°C for 4 hours and 24 hours, respectively, did not result in significant loss of radiolabel. But extending incubation with 10% serum to 24 hours led to a 5.2% loss of radiolabel. This loss was likely due to serum interaction as the same conjugate was stable in water during the same incubation period. Nevertheless, this loss of radiolabel should not appreciably affect the *in vivo* trafficking study of the radiolabeled micelles, as they are expected to quickly distribute into various organs and tissues within a couple of hours of administration.⁷⁻⁹

In order to characterize the effect of radiolabeling on micelle formation, the nonradioactive form of indium chloride was used to prepare the labeled polymer and DNA-containing micelles. The In-labeled DTPA-PEG-*b*-PPA did not show significant reduction in its DNA condensation ability and micelle formation, apparent from similar morphologies, sizes and zeta potentials measured for unlabeled and labeled micelles. Since the salt and serum stability profiles can be good indicators of *in vivo* stability of the micelles,⁶ we evaluated the complex stability of In-labeled micelles after incubation with salt and serum-containing medium using unlabeled micelles as the control. No DNA leakage was observed from the labeled micelles or unlabeled micelles. These studies collectively confirmed that this labeling protocol did not significantly influence the DNA-compaction ability of the labeled polymer; and the micelles formed with DNA exhibited similar size, surface charge, and stability as the unlabeled micelles under physiological ionic strength and in serum-containing medium.

Calibration and validation of the SPECT imaging analysis

The quantitative analysis of the radiolabeled carriers in animals using SPECT imaging can be significantly influenced by a number of experimental parameters, including photon attenuation, scattering, collimator-detector blurring, and partial volume effect, etc.²⁶ It is essential to compensate these effects to ensure a reliable quantitative analysis. We have generated a phantom to correct for the physical perturbations and calibrate the SPECT imaging quantification parameter. The similar data sets generated by parallel biodistribution (gamma-counting) and pharmacokinetic experiments (SPECT/CT imaging) using the same radiolabeled micelles following intravenous administration in rats demonstrated the accuracy of using SPECT/CT imaging data to generate pharmacokinetic and biodistribution profiles.

Biodistribution and pharmacokinetics of PEG-*b*-PPA/DNA micelles after intravenous infusion

After intravenous infusion, uptake of the DNA micelles in the liver occurred within minutes after infusion began and continued

to increase with infusion of the micelles (Figure 3c). Most of the radioactivity was gradually cleared from the blood (Figure 3a). A minor uptake in spleen and kidney may be due to the uptake by macrophages in these organs. Surprisingly, no significant accumulation in lung was observed. This can be explained by the improved colloidal stability of micellar nanoparticles, which could reduce particle agglomeration following contact with serum protein and subsequently be filtered by fine capillary bed of lung (Figure 3b).¹⁶

Pharmacokinetics of PEG-*b*-PPA/DNA micelles after hydrodynamic injection

Hydrodynamic injection has been used to achieve liver-specific delivery of plasmid DNA. It involves rapid bolus injection of large volume (10% of body weight) and high pressure as a driving force for DNA distribution to the liver. Earlier investigation reported that the majority of plasmid DNA uptake and transgene expression occur in the liver (>90%) after hydrodynamic injection.²² Due to this characteristic, hydrodynamic injection is regarded as a benchmark in the liver-targeted gene delivery. Consistent with earlier reports for plasmid DNA delivery, the majority of injected micelles rapidly accumulated in the liver, whereas minor fractions were found in the spleen and kidney after hydrodynamic injection of radiolabeled DNA micelles (Figure 4b,c). As a result of this efficient liver accumulation, very low fraction of micelles was detected in the blood after hydrodynamic injection.

Pharmacokinetics of PEG-*b*-PPA/DNA micelles after intrabiliary infusion

Although highly efficient for liver-targeted delivery, the requirement of rapid injection of a large volume of solution makes it less practical for clinical application. The retrograde intrabiliary infusion has been developed as an alternative to provide a direct delivery route to reach parenchymal hepatocytes and avoid the first contact with Kupffer cells.^{6,27–29} The large surface area and broadly distributed biliary system provides great access to nearly all the hepatocytes in liver parenchyma thus facilitating hepatocyte-specific delivery. Here, we showed that radiolabeled micelles administered by intrabiliary infusion were extensively retained by the liver, whereas the exposure to other organs was negligible (Figure 4e,f). These results are consistent with our earlier findings that infusion of DNA/chitosan nanoparticles^{27,28} and PEG-*b*-PPA/DNA^{6,21} micellar nanoparticles through intrabiliary infusion results in the highest liver-specific transgene expression with very low levels of gene expression in other organs.^{21,28,29} Further analysis of the pharmacokinetics of micelles in the liver after different modes of administration showed that the highest efficiency of liver-targeted delivery of micelles was obtained with intrabiliary infusion. In addition, micelle concentration in the liver reached the plateau by the end of intrabiliary infusion (Figure 5), suggesting that the distribution of micelles to the liver occurred rapidly through intrabiliary infusion compared to other routes evaluated, and the micellar nanoparticles were effectively retained in the liver with low distribution to other organs. It is worth noting that the SPECT/CT analysis conducted here is not sensitive enough to reveal cellular distributions of the nanoparticles *in vivo*. Our previous report described cellular distribution of nanoparticles after

intrabiliary infusion.²⁷ Although the cellular distribution of nanoparticles was found to be moderately dependent on the gene carrier, the predominant cell type associated with nanoparticles was the hepatocyte; nanoparticle uptake by Kupffer cells or endothelial cells was rare events as observed on tissue sections. We anticipate similar cellular distribution characteristics apply to the micellar nanoparticles studied here.

The two-compartment modeling of pharmacokinetics after intrabiliary infusion helped to further understand the mechanism of micelle delivery to the liver. Besides showing the rapid partition and retention of micelles in the liver, the model revealed high average micelle concentrations in the liver during (A) and post the infusion phase (B). Only a small fraction of the infused dose leaked out of the liver during the infusion phase ($\alpha = 0.30 \pm 0.05/\text{minute}$). The leakage of nanoparticles might be driven by the mild pressure applied to infused micelle solution, causing slight opening of tight junctions between hepatocytes and leakage of micelles through liver sinusoidal fenestrae to the blood compartment.³⁰ This finding also confirmed our previously observed transgene expression in other organs following intrabiliary infusion, albeit at much lower levels.^{28,29} The model also suggested that once micelles were taken up by the liver, low subsequent distribution from the liver to the blood or other organs occurred as indicated by the low elimination rate constant in postinfusion phase. These analyses further confirm the advantage of using intrabiliary infusion as the route for liver-targeted delivery of nanoparticles, as this administration route can achieve even higher efficiency of liver-targeted delivery of nanoparticles than hydrodynamic injection. Furthermore, intrabiliary infusion can be adopted as a reasonably safe protocol through endoscopic retrograde cholangiopancreatography in clinical setting.³¹

In summary, the *in vivo* pharmaceutical kinetic profiles of radiolabeled PEG-*b*-PPA/DNA micelles after different routes of administration were compared using SPECT/CT imaging method. Administration of DNA-containing micelles by three different routes exhibited distinctly different pharmacokinetic and biodistribution profiles. The high temporal and spatial resolution offered by the SPECT/CT enabled estimation of characteristic trafficking patterns of micelles in various organs after different routes of injection. Using this information, a two-compartment model for intrabiliary infusion of micelles was constructed. According to the model, the majority of delivered micelles retained in the liver and very small fractions of micelles leaked out to the blood compartment during and after the infusion phase. Based on these imaging analyses, we conclude that intrabiliary infusion is an optimal administration modality for liver-targeted gene delivery using PEG-*b*-PPA/DNA micelles.

MATERIALS AND METHODS

Conjugation of *p*-SCN-Bn-DTPA to polymer. The PEG_{12k}-*b*-PPA_{68k} was synthesized and purified according to method reported previously.^{6,32} PEG-*b*-PPA was dissolved in pH 8.5 carbonate buffer (0.1 mol/l) containing 10 mmol/l EDTA to achieve 10 mmol/l concentration. 2-(4-Isothiocyantobenzyl)-diethylenetriaminepentaacetic acid (*p*-SCN-Bn-DTPA; Macrocylics, Dallas, TX) was dissolved in DMSO (Sigma-Aldrich, St. Louis, MO) at a concentration of 1 mg/ml, and various amount of the solution was added to react with PEG-*b*-PPA solution to achieve molar ratios of SCN groups in *p*-SCN-Bn-DTPA to amino groups in

PEG-*b*-PPA of 1, 2, 6, 10, and 20%. The mixture was vortexed and incubated for 24 hours at room temperature. After incubation, free DTPA was removed from the polymer by ultracentrifugation. The reaction mixture was placed in Amicon Ultra-4 spin columns with molecular weight cutoff of 10 kDa (Millipore, Billerica, MA), diluted to 4 ml with pH 8.5 carbonate buffer (0.1 mol/l) containing 10 mmol/l EDTA (Sigma-Aldrich) and filtered at 3,000 r.p.m. for 30 minutes. The procedure is repeated three times, and then the buffer was replaced by ultrapure water using the same method. After purification, the conjugated polymer solution was collected and the concentration was adjusted to 10 mmol/l using ultrapure water. The DTPA-conjugated polymer solution was sterilized by filtration through 0.22- μ m filter and stored at -20°C till further use. For ^1H -NMR analysis, the unconjugated polymer and DTPA-conjugated polymer solution was freeze-dried (Labconco, Kansas City, MO) and reconstituted with D_2O and analyzed on Bruker 400-MHz NMR (Bruker, Billerica, MA).

Radiolabeling of PEG_{12k}-*b*-PPA_{68k} polymer. The radiolabeling of PEG_{12k}-*b*-PPA_{68k} polymer was carried out in 0.1 mol/l sodium acetate buffer (pH 5.0). The acetate buffer was mixed with polymer solution at 1:1 vol/vol ratio followed by addition of $^{111}\text{InCl}_3$ (3.7–18.5 MBq) (MDS Nordion, Ottawa, ON, Canada). The mixture was degassed using nitrogen gas purging. The mixture was incubated at 50°C for 60 minutes. The unlabeled radioactivity was complexed by addition of 5–20 μl of EDTA solution, mixed and reaction mixture was incubated again for 10 minutes at 50°C . Purification of radiolabeled polymer was carried out by centrifugal filtration using Amicon Ultra-0.5 filter unit with molecular weight cutoff of 10 kDa (Millipore). The filtration was repeated three times using water as diluent. The purified radiolabeled polymer was purged with nitrogen and stored at -20°C until use. For physicochemical analysis of DNA micelles, nonradioactive indium chloride (Sigma-Aldrich) was used instead of $^{111}\text{InCl}_3$ according to the same protocol.

Determination of radiolabeling efficiency and radiochemical purity. The radiolabeling efficiency was determined by thin-layer chromatography reported earlier³³ with minor modification. The radiolabeled formulation was spotted on a thin-layer chromatography plate (EM Science, Gibbstown, NJ) and developed using 10 mmol/l EDTA solution as the mobile phase. Solvent was allowed to travel 10 cm from the origin. The plate was removed, dried, and cut in two equal halves. The radioactivity associated with the plates was read in automated gamma counter (1282 Compugamma CS; Pharmacia/LKB Nuclear Inc, Gaithersburg, MD) as counts per minute. Radioactivity corresponding to the lower half was regarded as (polymer) bound activity while the radioactivity corresponding to the upper half was regarded as unbound (free) activity (R_f of EDTA-complexed $^{111}\text{In} = 1$). Stability of radiolabeled complex was determined by monitoring radiolabeling efficiency for up to 24 hours at 37°C in water and in 10% serum. The radiolabeling efficiency of the purified radiolabeled polymer at 0 hours was taken as control (100%) based on which radiolabeling of other stability of other samples was evaluated.

$$\text{Percent radiolabeling efficiency} = \frac{\text{Polymer bound radioactivity}}{\text{Total radioactivity}} \times 100\%$$

For radiochemical purity estimation of radiolabeled polymer, high-performance size exclusion liquid chromatography was performed using a Phenomenex BioSep-SEC-S2000 size exclusion column (300 \times 7.8 mm) on a Varian Prostar System (Palo Alto, CA), equipped with simultaneous UV-radioactivity detector, a model 490 UV absorbance detector at 260 nm and a Bioscan NaI scintillation detector connected to a Bioscan Flow-count system (Bioscan, Washington, DC). The mobile phase was 0.5 mol/l acetate buffer and the flow rate was 0.5 ml/minute.

Preparation of PEG-*b*-PPA/DNA micellar nanoparticles. The equal volume of (radiolabeled or nonradiolabeled) polymer solution and DNA

solution (100 $\mu\text{g}/\text{ml}$) in water were mixed at an N/P ratio of 10 (nitrogen of polymer to phosphate of DNA ratio) with gentle pipetting. The mixture was incubated at room temperature for 15 minutes before use.

Physicochemical characterization of DNA micelles. The nanoparticle size was measured by dynamic light scattering on a ZS90 Zetasizer (Malvern Instruments, Southborough, MA) at 25°C at a 90° scattering angle after diluted appropriately in water. The mean hydrodynamic diameter was determined by cumulative analysis. The zeta potential measurements were performed using an aqueous dip cell in the automatic mode. The particle size and zeta potential measurements were repeated three times for each sample, and the data were reported as the mean \pm SD of mean.

Transmission electron microscopy. About 10 μl of nanoparticle dispersion was added onto a ionized 400-mesh nickel Formvar/Carbon film TEM grid (Electron Microscope Sciences, Hatfield, PA) and air-dried. Aqueous uronic acid solution (1%, wt/vol) was used as negative staining agent. Grids were treated with 2 μl of uranium acetate solution and air-dried. The TEM images of stained indium-labeled and unlabeled DNA micelles were recorded on an FEI Tecnai 12 Twin 120 kV TEM (FEI, Hillsboro, OR).

Gel retardation assay. The indium-labeled and unlabeled DNA micelles were mixed with NaCl solution (final concentration, 0.15 mol/l of NaCl) or serum (final concentration, 10% of serum) for 1 hour at 37°C . The samples (10 μl) were mixed with Blue/Orange-Loading Dye (Promega, Madison, WI) and analyzed by electrophoresis on 1% agarose gel containing 2 μl of ethidium bromide (0.5 mg/ml; Sigma-Aldrich). Electrophoresis was carried out at 90 V in TAE buffer for 45 minutes. The DNA bands were visualized and recorded under a UV light (Eagle Eye II; Stratagene, La Jolla, CA).

Biodistribution profile of PEG-*b*-PPA/DNA nanoparticles. All *in vivo* experimental procedures were approved by the Johns Hopkins University Institutional Animal Care and Use Committee. Biodistribution studies were carried out in Female Wistar rats (Harlan Laboratories, Frederick, MD, 6–8 weeks old, 200–250 g, $n = 4$ for each group). Rats were housed under standard conditions and had free access to water and were fed standard laboratory chow. Animals were anesthetized by intramuscular injection of Ketamine hydrochloride (50 mg/kg; Bioniche Pharma USA, LLC, Lake Forest, IL) and Xylazine hydrochloride (10 mg/kg; IVX Animal Health, St Joseph, MO).

The radiolabeled micelles equivalent to 20 μg of DNA (~ 1.11 MBq) were diluted to 4 ml with 5% wt/vol sterile dextrose solution. The micelles were infused through tail vein using injection pump at the rate of 0.2 ml/minutes. For pharmacokinetic profiling of the micelles, the blood was collected through retro-orbital plexus at predetermined time intervals. At the end of 2 hours, the animals were sacrificed, and the heart, spleen, lungs, stomach, liver, small intestine, and kidneys were isolated. The organs were washed with water, blot-dried, and weighed. The radioactivity (in counts per minute) in each weighed organ fractions (100–200 mg, multiple slices were read per organ) was determined using gamma counter (1282 Compugamma CS). The percent of injected dose in an organ was calculated using the following equation.

$$\text{Percent of injected dose} = \frac{\text{Total activity in the organ}}{\text{Total injected dose}} \times 100\%$$

SPECT/CT imaging. SPECT and CT images were acquired using the Gamma Medica-Ideas X-SPECT small animal imaging system (Gamma Medica Ideas, Northridge, CA). Isoflurane/oxygen mixture was used as anesthetics for induction and maintenance throughout the imaging procedure. The indium-labeled micelles (18.5–37 MBq) equivalent to 20 μg of DNA was used and diluted appropriately using 5% sterile dextrose solution to 4 ml. The intravenous and bile duct infusion was carried out at 0.2 ml/minutes through tail vein and common bile duct, respectively. In case of hydrodynamic injection, 20 ml of radiolabeled micelles containing 20 μg

of plasmid DNA were injected through tail vein in 15 seconds (80 ml/minute). For intravenous and bile duct infusion, the radiolabeled micelles were administered simultaneously while scanning. However, for hydrodynamic injection, the rapid injection of high volume causes hydrodynamic shock to the animal; therefore the SPECT scans were initiated at 2 minutes after the injection to allow the animals to recover.

Each rat was first subjected to a series of dynamic SPECT scans at 10 time points, i.e., four scans at 5-minute intervals, followed by two 10-minute intervals and four 20-minute intervals. The acquisition time at each time point equaled to the time interval. The scanning region was adjusted to cover the organs from lungs to kidneys. These scans were followed by a whole-body spiral SPECT scan and a whole-body CT scan. In the SPECT scans, the dual-head detectors were fitted with medium-energy single-pinhole collimators with aperture size of 1.0 mm, and step-and-shot rotation for 64 projection angles 360°. The radius-of-rotation was set at 6.5 cm, which provided a field-of-view of 7.5 cm to cover the rat body from lung to kidney. The whole-body spiral SPECT was performed 2 hours after the dynamic SPECT scans. The dual-detectors took three 360° rotations. During each rotation, 64 pinhole projections each with 20-second acquisition time were obtained while the bed moved axially with a step size of 1.4 mm. The 64 frames of acquired SPECT projection images in 80 × 80 matrices with 1.5-mm bin size were reconstructed using a 3-D OS-EM algorithm with two iterations and four subsets to generate a 3-D SPECT image in 80 × 80 × 80 matrix with 1.0 mm pixel size.

The CT scans were obtained with a magnification of 1.5 and the tube setting of 75 kVp and 0.225 mA. A total of 512 projections over 360° were acquired with 0.2 second/projection in a 2-minute continuous rotation mode. The 512 frames of acquired CT projection images in 1,184 × 1,120 matrices with 0.1-mm bin size were reconstructed using the Feldkamp cone-beam algorithm to generate a 3-D CT image in 512 × 512 × 1,000 with 0.17 mm pixel size.

The reconstructed SPECT and CT images were coregistered with each other using a rigid-body transformation with precalibrated transformation parameters. To quantify the uptake of radiolabeled micelles in specific organ, the registered SPECT and CT images were analyzed using the open source of AMIDE (v0.9.1 SourceForge.net). A 3-D region-of-interest was manually drawn to encompass the radioactivity uptake in the organ whose boundary was delineated in the 3-D CT images. Separate region-of-interests were drawn for the radioactivity uptakes in the lung, heart, liver, spleen, stomach, and left and right kidneys. A region-of-interest was drawn within the left ventricle to calculate the average uptake in the blood. The mean SPECT image intensity within each region-of-interest was calculated and then transferred into mean radioactivity by multiplying a precalculated calibration factor, which was generated from a phantom experiment (see the **Supplementary Figure S4, Supplementary Tables S1 and S2, and Supplementary Materials and Methods** for calibration factor calculation). The %ID/g was calculated using the following equation:

$$\text{Percentage of injected dose/gram of tissue} = \frac{\text{Mean activity in the ROI (MBq/g)}}{\text{Total injected dose (MBq)}} \times 100\%$$

and was plotted as a function of time postinjection. The data at each time point during the dynamic SPECT acquisition was an average over a scan period equaled to the time interval. For example, the first data at the 2.5-minute time point was obtained from the first 5-minute scan and the second data at 7.5-minute time point was obtained from the second 5-minute scan, etc. The % injected dose/g of tissue at the 110-minute time point (last time point) was converted to total dose/organ by multiplying the organ weight to generate the biodistribution profile of the specific organ.

We chose to have smaller field-of-view covering major organs from lung to kidneys (**Figures 3 and 4**), which are major organs of involved in DNA nanoparticle transport based on the biodistribution analysis (**Figure 3b**), to get more accurate measurement of radioactivity without

compromising the sensitivity. This has resulted in leaving other organs (mainly bladder) out of view. Our data revealed that the total amount of micelles distributed to the major organs, which can be reliably quantified using our SPECT imaging protocol, was about 95% of the injected dose, whereas the small fraction (~5%) of micelles was left unaccounted in remaining body organs.

Data analysis. All the data in tables and figures were expressed as mean ± SD of mean. Statistical analysis was performed using the one-way ANOVA with Tukey–Kramer HSD and Student's *t*-tests using the Graphpad Prism 5 software (Graphpad Software, La Jolla, CA). A *P* value of <0.05 was used as a criterion for statistical significance. The pharmacokinetic and compartmental analysis was calculated from the respective average concentration values using a published PKsolver program.²⁵

SUPPLEMENTARY MATERIAL

Figure S1. Schematic representation of radiolabeling of PEG-*b*-PPA.

Figure S2. The ¹H-NMR spectra of PEG_{12k}-*b*-PPA_{68k} and DTPA-Bn-PEG_{12k}-*b*-PPA_{68k}.

Figure S3. HPLC chromatograms of purified ¹¹¹In-labeled DTPA-Bn-PEG_{12k}-*b*-PPA_{68k} analyzed by UV and radioactivity dual detectors.

Figure S4. The SPECT/CT images of a rat-size cylindrical phantom and the rat showing the ¹¹¹In-filled capillaries with the same radioactivities placed in different parts of rat body.

Table S1. The results of calibration factor calculation in the phantom study.

Table S2. The comparison between the calculated and measured radioactivities in the rat.

Video 1. The 3-D nanoparticle distribution at 2 hours after intravenous infusion rendered from whole-body scan images.

Video 2. The 3-D nanoparticle distribution at 2 hours after hydrodynamic injection rendered from whole-body scan images.

Video 3. The 3-D nanoparticle distribution at 2 hours after intrabiliary infusion rendered from whole-body scan images.

Supplementary Materials and Methods.

ACKNOWLEDGMENTS

The authors thank James Fox and Gilbert Green of BRB Molecular Imaging Center, Gary Huang of Department of Radiology, Deng Pan and John-Michael Williford at Department of Biomedical Engineering, Johns Hopkins School of Medicine, for their technical assistance and helpful discussion. We thank Yun Zhou of Department of Radiology, Johns Hopkins School of Medicine for the helpful discussion on the compartmental modeling. We acknowledge the support of NIH/NIDDK through Grant DK068399 (H.-Q.M.), NIH/NIGMS through Grant GM073937 (H.-Q.M.), NIH/NCI through Grant CA92871 (M.P.) and Institute of Nanobiotechnology, Johns Hopkins University (H.-Q.M. and D.L.K.).

REFERENCES

1. Midoux, P, Breuzard, G, Gomez, JP and Pichon, C (2008). Polymer-based gene delivery: a current review on the uptake and intracellular trafficking of polyplexes. *Curr Gene Ther* **8**: 335–352.
2. Sun, X and Zhang, N (2010). Cationic polymer optimization for efficient gene delivery. *Mini Rev Med Chem* **10**: 108–125.
3. Mao, HQ and Leong, KW (2005). Design of polyphosphoester-DNA nanoparticles for non-viral gene delivery. *Adv Genet* **53**: 275–306.
4. Zhang, XQ, Wang, XL, Huang, SW, Zhuo, RX, Liu, ZL, Mao, HQ *et al.* (2005). *In vitro* gene delivery using polyamidoamine dendrimers with a trimesyl core. *Biomacromolecules* **6**: 341–350.
5. Wang, J, Gao, SJ, Zhang, PC, Wang, S, Mao, HQ and Leong, KW (2004). Polyphosphoramidate gene carriers: effect of charge group on gene transfer efficiency. *Gene Ther* **11**: 1001–1010.
6. Jiang, X, Dai, H, Ke, CY, Mo, X, Torbenson, MS, Li, Z *et al.* (2007). PEG-*b*-PPA/DNA micelles improve transgene expression in rat liver through intrabiliary infusion. *J Control Release* **122**: 297–304.
7. Nishikawa, M, Takakura, Y and Hashida, M (2005). Pharmacokinetics of plasmid DNA-based non-viral gene medicine. *Adv Genet* **53**: 47–68.
8. Mahato, RI, Kawabata, K, Takakura, Y and Hashida, M (1995). *In vivo* disposition characteristics of plasmid DNA complexed with cationic liposomes. *J Drug Target* **3**: 149–157.
9. Dash, PR, Read, ML, Barrett, LB, Wolfert, MA and Seymour, LW (1999). Factors affecting blood clearance and *in vivo* distribution of polyelectrolyte complexes for gene delivery. *Gene Ther* **6**: 643–650.

10. Nichol, CA, Yang, D, Humphrey, W, Ilgan, S, Tansey, W, Higuchi, T *et al.* (1999). Biodistribution and imaging of polyethyleneimine - A gene delivery agent. *Drug Deliv* **6**: 187–194.
11. Zhou, QH, Wu, C, Manickam, DS and Oupický, D (2009). Evaluation of pharmacokinetics of bioreducible gene delivery vectors by real-time PCR. *Pharm Res* **26**: 1581–1589.
12. Nichol, C and Kim, EE (2001). Molecular imaging and gene therapy. *J Nucl Med* **42**: 1368–1374.
13. Weissleder, R and Mahmood, U (2001). Molecular imaging. *Radiology* **219**: 316–333.
14. Palladino, F, Canadè, A, Bianchi, A, Lesti, G, Antoniol, OM, Macis, G *et al.* (2003). Molecular imaging: state of the art. *Rays* **28**: 45–61.
15. Morille, M, Montier, T, Legras, P, Carmoy, N, Brodin, P, Pitard, B *et al.* (2010). Long-circulating DNA lipid nanocapsules as new vector for passive tumor targeting. *Biomaterials* **31**: 321–329.
16. Zintchenko, A, Sussha, AS, Concia, M, Feldmann, J, Wagner, E, Rogach, AL *et al.* (2009). Drug nanocarriers labeled with near-infrared-emitting quantum dots (quantoplexes): imaging fast dynamics of distribution in living animals. *Mol Ther* **17**: 1849–1856.
17. Franc, BL, Acton, PD, Mari, C and Hasegawa, BH (2008). Small-animal SPECT and SPECT/CT: important tools for preclinical investigation. *J Nucl Med* **49**: 1651–1663.
18. Townsend, DW (2008). Dual-modality imaging: combining anatomy and function. *J Nucl Med* **49**: 938–955.
19. Maurer, AH (2008). Combined imaging modalities: PET/CT and SPECT/CT. *Health Phys* **95**: 571–576.
20. Kasuya, T and Kuroda, S (2009). Nanoparticles for human liver-specific drug and gene delivery systems: *in vitro* and *in vivo* advances. *Expert Opin Drug Deliv* **6**: 39–52.
21. Jiang, X, Leong, D, Ren, Y, Li, Z, Torbenson, MS and Mao, HQ (2011). String-Like Micellar Nanoparticles Formed by Complexation of PEG-b-PPA and Plasmid DNA and Their Transfection Efficiency. *Pharm Res* **28**: 1317–1327.
22. Herweijer, H and Wolff, JA (2007). Gene therapy progress and prospects: hydrodynamic gene delivery. *Gene Ther* **14**: 99–107.
23. Dipiro, JT, Spruill, WJ, Wade, WE, Blouin, RA and Pruemer, JM (2010). *Concepts in Clinical Pharmacokinetics*. 5th edn. American Society of Health-System Pharmacists: Bethesda, MD.
24. Metzler, CM (1971). Usefulness of the two-compartment open model in pharmacokinetics. *J Am Stat Assoc* **66**: 49–53.
25. Zhang, Y, Huo, M, Zhou, J and Xie, S (2010). PKSolver: An add-in program for pharmacokinetic and pharmacodynamic data analysis in Microsoft Excel. *Comput Methods Programs Biomed* **99**: 306–314.
26. Hwang, AB, Franc, BL, Gullberg, GT and Hasegawa, BH (2008). Assessment of the sources of error affecting the quantitative accuracy of SPECT imaging in small animals. *Phys Med Biol* **53**: 2233–2252.
27. Dai, H, Jiang, X, Tan, GC, Chen, Y, Torbenson, M, Leong, KW *et al.* (2006). Chitosan-DNA nanoparticles delivered by intrabiliary infusion enhance liver-targeted gene delivery. *Int J Nanomedicine* **1**: 507–522.
28. Jiang, X, Dai, H, Leong, KW, Goh, SH, Mao, HQ and Yang, YY (2006). Chitosan-g-PEG/DNA complexes deliver gene to the rat liver via intrabiliary and intraportal infusions. *J Gene Med* **8**: 477–487.
29. Otsuka, M, Baru, M, Delriviere, L, Talpe, S, Nur, I and Gianello, P (2000). *In vivo* liver-directed gene transfer in rats and pigs with large anionic multilamellar liposomes: routes of administration and effects of surgical manipulations on transfection efficiency. *J Drug Target* **8**: 267–279.
30. Hu, J, Zhang, X, Dong, X, Collins, L, Sawyer, GJ and Fabre, JW (2005). A remarkable permeability of canalicular tight junctions might facilitate retrograde, non-viral gene delivery to the liver via the bile duct. *Gut* **54**: 1473–1479.
31. Xie, X, Forsmark, CE and Lau, JY (2000). Effect of bile and pancreatic juice on adenoviral-mediated gene delivery: implications on the feasibility of gene delivery through ERCP. *Dig Dis Sci* **45**: 230–236.
32. Jiang, X, Zheng, Y, Chen, HH, Leong, KW, Wang, TH and Mao, HQ (2010). Dual-sensitive micellar nanoparticles regulate DNA unpacking and enhance gene-delivery efficiency. *Adv Mater Weinheim* **22**: 2556–2560.
33. Patil, RR, Gaikwad, RV, Samad, A and Devarajan, PV (2008). Role of lipids in enhancing splenic uptake of polymer-lipid (LIPOMER) nanoparticles. *J Biomed Nanotechnol* **4**: 359–366.